All-Silicon Terahertz Planar Horn Antenna

Jie Liang, Weijie Gao, Harrison Lees, *Student Member, IEEE*, and Withawat Withayachumnankul, *Senior Member, IEEE*

***Abstract*—In this letter, we propose an integrated all-silicon 2-D horn antenna operating over 220 to 330 GHz (WR-3 band). This endfire antenna is designed for full integration with a substrateless all-dielectric terahertz frontend. The antenna supports two orthogonal fundamental modes of guided waves with in-plane and out-of-plane polarizations. By introducing a 2-D effective-medium dielectric lens on the same platform, the antenna realized gain together with the free-space impedance matching is enhanced allowing for a broadband operation with a fractional impedance bandwidth of 40% on a compact footprint. The fabricated antenna is experimentally validated with measured realized gain ranging from 11.2 to 14.2 dBi for the in-plane polarization and 10.5–15.0 dBi for the out-of-plane polarization across the entire WR-3 band. We foresee that this all-dielectric horn antenna together with the integrated highly efficient platform can be adopted in beyond 5G communications.**

***Index Terms*—2-D horn antenna, dielectric lens, dielectric waveguide, effective medium, terahertz communications.**

I. Introduction

RAPIDLY growing data usage in various high-quality multimedia has raised demands in wireless communications with high channel capacities [1]–[3]. The terahertz spectrum with vast available bandwidth exhibits great potentials to promote beyond 5G communications. However, due to the limited source power and high free-space path loss, it is critical to develop highly efficient frontends for terahertz wireless applications. Importantly, antennas with high gain, high efficiency, and broad bandwidth are critical for these terahertz frontends. To build such antennas, material properties and manufacturability must be considered. It is challenging to directly scale existing metallic microwave antennas up to the terahertz frequencies due to their significant ohmic losses and increasing manufacturing complexity at terahertz frequencies [4]–[11]. Although metallic horn antennas feature high efficiency due to the low current density in metal [12], the increasing manufacturing complexity and cost together with the bulky structures limit their integrability.

Manuscript received April 16, 2021; revised June 15, 2021; accepted June 29, 2021. Date of publication July 2, 2021; date of current version November 16, 2021. This work was supported by the Australian Research Council Discovery Project under Grant ARC DP180103561. *(Jie Liang and Weijie Gao contributed equally to this work.) (Corresponding authors: Jie Liang; Weijie Gao.)*

Jie Liang is with the Terahertz Engineering Laboratory, University of Adelaide, Adelaide, SA 5005, Australia, and also with the School of Computer Science, University of Adelaide, Adelaide, SA 5005, Australia (e-mail: jie.liang02@student.adelaide.edu.au).

Weijie Gao, Harrison Lees, and Withawat Withayachumnankul are with the Terahertz Engineering Laboratory, School of Electrical and Electronic Engineering, University of Adelaide, Adelaide, SA 5005, Australia (e-mail: weijie.gao@adelaide.edu.au; harrison.lees@adelaide.edu.au; withawat.withayachumnankul@adelaide.edu.au).

Digital Object Identifier 10.1109/LAWP.2021.3094310

To enable antenna integration, a terahertz H-plane horn antenna surrounded by metallic photonic crystal rod array was proposed [13], despite its bandwidth limited by the photonic bandgap effect. Alternatively, an integrated dielectric resonator antenna with endfire radiation was reported [14]. This antenna was implemented on a 2-D photonic crystal waveguide platform made of only silicon to eliminate the ohmic loss with a maximum realized gain of 10.6 dBi. However, due to the resonance nature of the antenna, its fractional bandwidth was only 6% over 311–331 GHz. To further enhance the bandwidth and realized gain, an all-silicon rod antenna array [15] and Luneburg lens [16] based on the same platform were reported. There, measured realized gains above 20 dBi were achieved across 315–390 GHz with a relative bandwidth of 21%. In essence, all these antennas integrated with the photonic crystal platform have relatively narrow bandwidth with high in-band dispersion and can support only one polarization, rooted in the intrinsic properties of photonic bandgap structures [3].

To this end, all-silicon effective-medium-clad dielectric waveguides together with various fundamental building blocks have been proposed by our group as an integrated platform for terahertz frontends [17], [18]. This substrateless platform features extremely low loss, low dispersion, and broad bandwidth, while supporting two orthogonal fundamental modes, namely E_{11}^{x} or in-plane and E_{11}^{y} or out-of-plane modes. The effective medium that supports the waveguide is realized by periodically perforating a silicon slab with subwavelength spacing. The relative permittivity of this effective medium can be flexibly controlled by adjusting the configuration of this subwavelength hole array. With such benefits, various terahertz integrated devices can be built on this platform to inherit high efficiency and broad bandwidth.

In this letter, we propose a planar horn antenna implemented onto this terahertz integrated platform over 220–330 GHz. The proposed antenna consists of a flaring section to increase the aperture size and an effective-medium lens to enhance the antenna realized gain together with the impedance matching to free space. The proposed all-silicon antenna has an extremely high efficiency nearly 100%. Compared to the rod-array antenna fed by a photonic crystal waveguide [15], the proposed design has a comparable efficiency but around a twofold increase in the fractional bandwidth owing to the performance of the feed waveguide. Importantly, the lens part synthesizes the functions of wavefront flattening together with impedance matching leading to a compact footprint. Compared to the dielectric microstrip-line-based horn antenna [19] supporting only out-of-plane polarization due to the waveguide mode restriction, the proposed

TABLE I
HOLE DIAMETERS FOR THE EFFECTIVE-MEDIUM DIELECTRIC LENS (d: HOLE DIAMETER WITH UNIT OF MICROMETER)

Row number	d_1	d_2	d_3	d_4	d_5	d_6	d_7	d_8	d_9	d_{10}	d_{11}	d_{12}	d_{13}	d_{14}	d_{15}	d_{16}	d_{17}
1 & 2	20	20	25	25	30	35	35	40	40	45	45	50	50	55	55	60	60
3 & 4	20	25	25	30	35	35	40	40	45	45	50	50	55	55	60	60	65
5 & 6	25	25	30	35	35	40	40	45	45	50	50	55	55	60	60	65	65
7 & 8	25	30	35	35	40	40	45	45	50	50	55	55	60	60	65	65	70
9 & 10	30	35	35	40	40	45	45	50	50	55	55	60	60	65	65	70	70
11 & 12	40	40	44	44	48	48	52	52	56	60	60	60	60	64	64	68	68
13 & 14	60	60	63	63	66	66	69	69	76	76	76	76	78	78	81	81	84
15 & 16	80	80	82	82	84	84	86	86	88	88	90	90	92	92	94	94	96

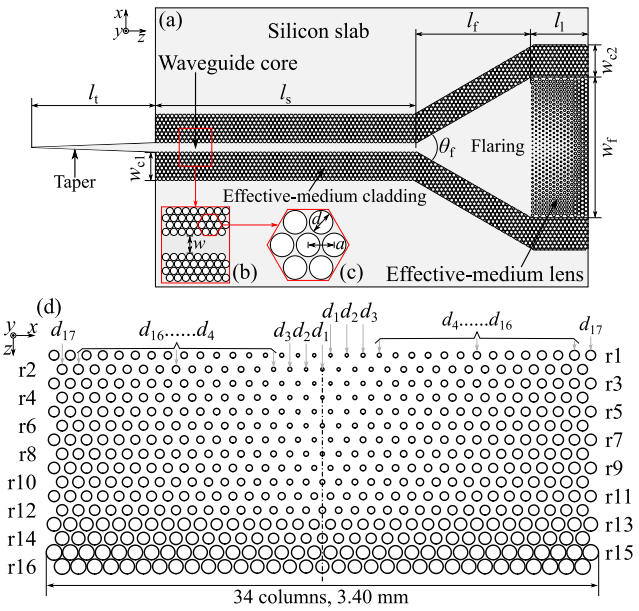

Fig. 1. Schematic of all-silicon 2-D horn antenna. All components are defined by through holes in a single silicon slab. (a) Antenna model. (b) Effective-medium-clad dielectric waveguide as a feed. (c) Effective-medium cladding in hexagonal lattice. (d) Effective-medium lens. The taper is for matched coupling from the hollow waveguide to the antenna in both simulation and measurement. Here, $l_t = 3.00$ mm, $l_s = 6.30$ mm, $l_f = 2.88$ mm, $l_l = 1.39$ mm, $w = 0.225$ mm, $w_f = 3.40$ mm, $w_{c1} = 0.69$ mm, $w_{c2} = 0.78$ mm, $\theta_f \approx 60°$, $a = 0.1$ mm, and $d = 0.09$ mm. The detailed dimensions of the lens can be found in Table I.

antenna can support both E_{11}^x and E_{11}^y guided modes resulting in radiation with orthogonal polarizations promising applications that require polarization diversity to increase wireless channel capacities.

II. ANTENNA DESIGN

As shown in Fig. 1(a), the antenna consists of an effective-medium-clad waveguide as a feed, a flare section, and a 2-D effective-medium lens. The lens and the claddings are realized by subwavelength perforation in hexagonal lattices, as shown in Fig. 1(b) and (c), specifically chosen for mechanical robustness. Accordingly, the relative permittivities of these perforated components can be controlled by varying the hole configuration, i.e., the perforation period a and hole diameter d, based on the Maxwell-Garnet effective medium theory [20]. By properly designing the lens with a spatially varying effective permittivity, the cylindrical wavefront emerging from the flaring section can be flattened, while a good impedance matching between the antenna and free space can be achieved allowing for broad gain and impedance bandwidths. To achieve high efficiency, the whole structure is built into a 250-μm-thick high-resistivity float-zone silicon wafer with a resistivity >10 kΩ-cm [17], [18]. This silicon exhibits a relative permittivity of $\epsilon_{\rm Si} = 11.68$ and loss tangent of 3×10^{-5} within the operation frequency range. Float-zone silicon has much higher purity than that fabricated with other techniques. This is much needed for terahertz applications to minimize material dissipation [21].

As shown in Fig. 1(b) and (c), the waveguide core width w is 225 μm, while the effective medium claddings is with a lattice period $a = 100\,\mu$m, i.e., three times smaller than the guided wavelength and a hole diameter $d = 90\,\mu$m resulting in the relative permittivity tensor $(\epsilon_x, \epsilon_y, \epsilon_z)$ of (2.75, 3.83, 2.75) [18]. In this design, the horn antenna is in the form of an in-plane flare, to yield a large effective aperture and realized gain [13], [22]. However, enlarging the flaring angle and aperture too much will exacerbate the cylindrical wavefronts due to an increasing difference in the path lengths [15]. Thus, the antenna realized gain will be degraded. On the other hand, increasing the length of the flaring section can reduce the flaring angle hence maintaining a reasonably planar wavefront but with the sacrifice of structural compactness. Considering the tradeoff between the antenna realized gain and the structural compactness, the 2-D flaring section in this letter is designed as shown in Fig. 1, where the flaring length and width are selected as $l_f = 2.88$ mm and $w_f = 3.40$ mm, respectively, leading to a flaring angle of $\theta_f \approx 60°$. With such a flaring angle, the transition between the feed waveguide and the aperture is smooth with an aperture size about three wavelengths across.

To further enhance the antenna realized gain and the free-space impedance matching while maintaining the structural compactness, a 2-D effective medium dielectric lens is introduced. The lens design is based on the principle discussed in [15]. Specifically, an array of small holes leads to a higher modal index, which can increase the phase delay, while an array of larger holes can reduce the transit time. Therefore, to equalize the phase delay of the emerging cylindrical wavefront, as shown in Fig. 1(d), a gradient hole distribution is adopted along the x-axis, where the hole diameter is gradually increased from the center to the edges of the lens. Due to the low dispersion of the air-silicon effective medium and the guided modes, the lens can support broadband operation for both linear polarizations. Meanwhile, to achieve a good free-space impedance matching, the hole diameter is gradually increased along the z-axis leading to a decreased modal index towards free space. The subwavelength lattice period a is selected as 100 μm, while the minimum

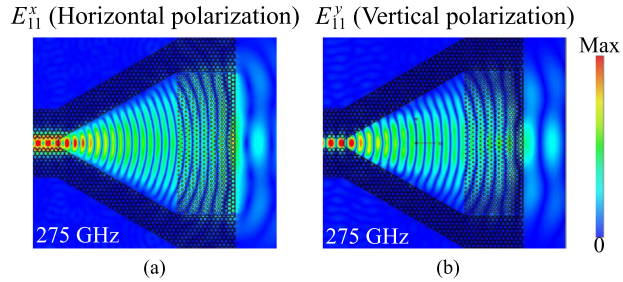

Fig. 2. Simulated instantaneous E-field amplitude distributions of the antenna. Amplitude distributions in linear scale for (a) E_{11}^x and (b) E_{11}^y modes at 275 GHz. All the amplitude plots are normalized to the same scale.

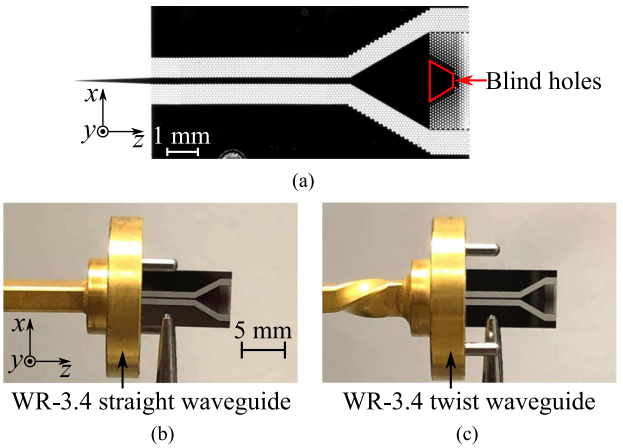

Fig. 3. Fabricated sample and measurement setup. (a) Microscopic image of the fabricated antenna. Antenna fed by (b) WR-3.4 straight waveguide and (c) WR-3.4 twist waveguide for the E_{11}^x and E_{11}^y modes.

hole diameter $d_{\min}$ is chosen as 20 μm, which is determined by the deep reactive ion-etching (DRIE) process. This configuration allows for a wide range of effective permittivity, resulting in a fine control for phase compensation and impedance matching. Our design goals include reflection coefficients below -10 dB and realized gains above 10 dBi with variations less than 3 dB across the whole WR-3 band for both polarizations.

To investigate the performance, the 3-D full-wave simulations are performed with CST Microwave Studio 2020, where a realistic loss tangent of 3×10^{-5} is employed for the silicon material. The simulated E-field distributions of the antenna for the two modes are shown in Fig. 2. It is observed that the waves emerging from the feed waveguide diverge in the flaring region, and then are gradually flattened when passing the effective-medium lens and being radiated into free space. The wave front of the E_{11}^y mode is slightly overcorrected due to the a small modal index difference between the two guided modes, which is expected to slightly reduce the overall gain.

III. Fabrication and Measurement

As shown in Fig. 3(a), the antenna is fabricated on a single high-resistivity float-zone silicon wafer with a thickness of 250 μm. The fabrication is based on standard deep reactive ion-etching (DRIE). The blind holes occur with the smallest holes around the center of lens. This is due to the achievable aspect ratio, i.e., the ratio between the hole depth and the width, which is limited to around 10:1 in this case. The measurements are carried out by using a Keysight vector network analyzer (VNA) with Virginia Diodes WR-3.4 extension modules spanning from 220 to 330 GHz. At the transmitter side, a WR-3.4 hollow waveguide with opening dimensions of 863.6 $\times$ 431.8 μm^2 feeds the antenna sample through the taper, while a WR-3.4 metallic horn antenna is adopted as a receiver. Specifically, the taper structure is inserted into the hollow waveguide for coupling, while an external holder is introduced to support the sample. For precise alignment, high-precision optical stages are used. It is noteworthy that the simulated results show that, for a perfectly aligned case, the coupling loss ranges from 1.3 to 0.2 dB for the E_{11}^x mode and from 0.8 to 0.2 dB for E_{11}^y mode over 220–330 GHz. The separation between the two antennas is 14 cm, beyond the far-field distance of around 4 cm at 330 GHz. As shown in Fig. 3(b) and (c), the sample is fed by a WR-3.4 straight waveguide for the E_{11}^x mode and a twist waveguide for the E_{11}^y mode. The yz-plane radiation pattern is measured by rotating the antenna in the yz plane with a pivot at the antenna end point. Additionally, the xz-plane radiation patterns can be measured by rotating the sample by 90°, while the straight and twist waveguides are swapped for the two modes. To measure the cross-polarized components in the two planes, a twist waveguide needs to be added or removed at the receiver in opposition to the twist involvement at the transmitter.

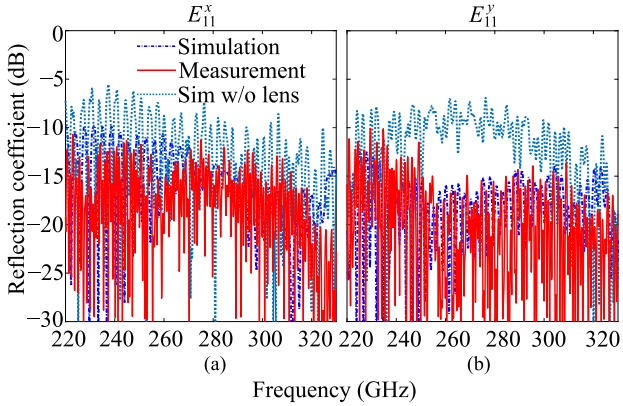

Fig. 4. Simulated and measured reflection coefficients for (a) E_{11}^x and (b) E_{11}^y modes. The simulation without lens is based on the model with absence of the effective lens, while the other parts remain unchanged.

Fig. 4 shows the simulated and measured reflection coefficients for the E_{11}^x and E_{11}^y modes, where the measurements reasonably agree with the simulations. For both polarizations, the simulated and measured reflection coefficients are well below -10 dB across the whole WR-3 band. Discontinuities in conjoined waveguide sections and external reflections cause rapid spectrum fluctuation in the measured results. It is shown that the reflection levels are reduced by more than 5 dB with the effective lens.

The simulated and measured radiation patterns for the two modes are illustrated in Fig. 5. For both polarizations, the measured 3-dB angular beamwidth in the xz plane is less than 20°, while it is around 85° in the yz plane for both polarizations. The fan beam is due to the unequal aperture dimensions in the

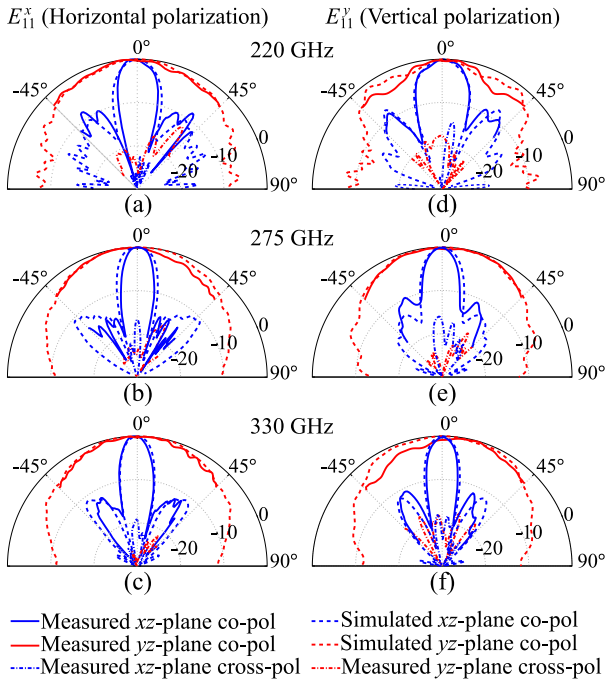

Fig. 5. Simulated and measured antenna radiation patterns for (a–c) the E_{11}^x and (d–f) E_{11}^y modes at 220, 275, and 330 GHz. The simulated cross-polarized components are not presented, since they are negligible due to the perfect symmetry of the antenna model. Due to the limited scanning angle of the setup, the antenna radiation patterns are measured from $-45°$ to 45°.

two planes, where the in-plane aperture is much larger than the out-of-plane one that is determined by the wafer thickness. The patterns for both modes are reasonably stable across the frequency range of the interest. The measured cross-polarization components below -10 dB are significantly higher than those in simulation. This cross-polarization level is similar to that measured in an effective-medium-clad waveguide, and was confirmed via simulation to be from a small misalignment to the feed rectangular waveguide [17]. It is observed that for the E_{11}^y mode, the measured radiation patterns in the yz plane at the edge frequencies have slightly larger discrepancies with the simulations. They are mainly caused by the sample imperfections, i.e., the actual wafer thickness is 5 μm less than the designated 250 μm and the holes are overetched by around 2.5 μm. These imperfections have been verified in simulation to cause similar effects in the radiation patterns.

As can be seen in Fig. 6, the measured realized gain ranges from 11.2 to 14.2 dBi for the E_{11}^x mode and from 10.5 to 15.0 dBi for the E_{11}^y mode over 220–330 GHz. It is observed that the measured gain for the E_{11}^y mode fluctuates over the entire band. Based on the free spectral range (FSR), the associated distance is approximately 1.2 cm, while the distance between the antenna tip and the taper structure is around 1.1 cm. In this case, we believe that the standing waves are caused by the impedance mismatch due to misalignment between the taper and the feed rectangular waveguide. Compared to the E_{11}^y mode, the E_{11}^x mode exhibits a lower sensitivity to the misalignment due to a better mode matching [18]. The increased realized gain with frequency is due to the larger effective aperture. The measured 3-dB realized gain bandwidth for the E_{11}^x mode is 110 GHz covering

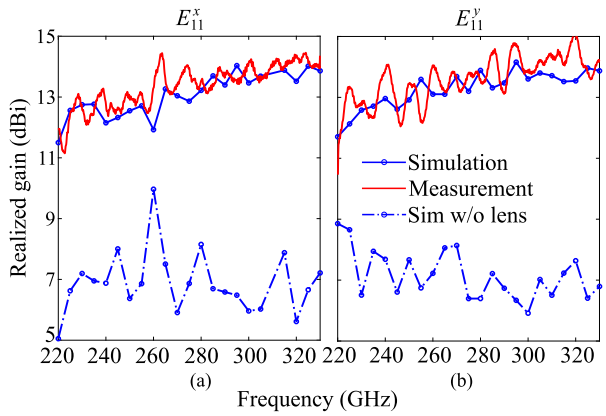

Fig. 6. Simulated and measured realized gains for (a) E_{11}^x and (b) E_{11}^y modes. The simulated realized gains are discrete with a sampling frequency of 5 GHz, while the lines are for visual guidance. To mitigate the noise introduced by misalignment, a smoothing function has been employed to process the measured gains with a sliding window covering 1 GHz.

the whole WR-3 band, while it is reduced to 107.8 GHz from 222.2 to 330 GHz for the E_{11}^y mode with realized gain ranging from 12.0 to 15.0 dBi. The results further show the effectiveness of the lens in performance enhancement. As illustrated in Fig. 6, the average realized gains are improved by around 6.0 dB for both polarizations compared with an identical antenna with no lens. It is worth to mention that confirmed by simulations, the blind holes around the center of lens have a negligible impact on the antenna performance attributed to the robustness of effective medium.

IV. Conclusion

In conclusion, an all-silicon planar horn antenna built on the effective-medium-clad dielectric waveguide platform has been proposed. The antenna operates in the WR-3 band while supporting two linear polarizations, resulting from the two orthogonal fundamental modes of guided waves. The efficiency of this antenna is near to 100% due to negligible dissipation of the float-zone intrinsic silicon. Attributed to the effective-medium lens, the antenna realized gains and impedance matching are significantly enhanced with a compact footprint. The experimental validation confirms a 40% fractional bandwidth for the E_{11}^x mode with reflection coefficient below -10 dB and realized gain ranging from 11.2 to 14.1 dBi over 220–330 GHz. Due to the fabrication and measurement tolerances, the 3-dB gain bandwidth for the E_{11}^y mode is slightly reduced with gain raging from 12.0 to 15.0 dBi. The overall antenna gain can be readily increased by scaling the aperture size together with the effective lens. It can be foreseen that such a dielectric horn antenna can be widely used in the next generation communications with a high channel capacity.

Acknowledgment

The authors would like to thank Dr. Wendy S. L. Lee for the assistances in the experiment. The samples were fabricated by Silicon Sensing Systems Japan Ltd. The Quadro P6000 GPU used for this research was contributed by NVIDIA Corporation.

REFERENCES

[1] T. Nagatsuma, G. Ducournau, and C. C. Renaud, "Advances in terahertz communications accelerated by photonics," *Nature Photon.*, vol. 10, no. 6, pp. 371–379, 2016.

[2] K. Sengupta, T. Nagatsuma, and D. M. Mittleman, "Terahertz integrated electronic and hybrid electronic-photonic systems," *Nature Electron.*, vol. 1, no. 12, pp. 622–635, 2018.

[3] W. Withayachumnankul, M. Fujita, and T. Nagatsuma, "Integrated silicon photonic crystals toward terahertz communications," *Adv. Opt. Mater.*, vol. 6, no. 16, pp. 1–7, 2018.

[4] Q. H. Abbasi, S. F. Jilani, A. Alomainy, and M. A. Imran, *Antennas and Propagation for 5G and Beyond*. London, U.K.: Inst. Eng. Technol., 2020.

[5] P. Zhao, Y. Liu, H. Lu, Y. Wu, and X. Lv, "Experimental realization of terahertz waveguide-fed circularly polarized double-fan-shaped slot antenna," *IEEE Antennas Wireless Propag. Lett.*, vol. 16, pp. 2066–2069, 2017.

[6] M. Alibakhshikenari *et al.*, "High-gain on-chip antenna design on silicon layer with aperture excitation for terahertz applications," *IEEE Antennas Wireless Propag. Lett.*, vol. 19, no. 9, pp. 1576–1580, Jul. 2020.

[7] Y. Dong, P. Liu, D. Yu, G. Li, and F. Tao, "Dual-band reconfigurable terahertz patch antenna with graphene-stack-based backing cavity," *IEEE Antennas Wireless Propag. Lett.*, vol. 15, pp. 1541–1544, 2016.

[8] H. Zhu, Y. Zhang, C. Wu, F. Xiao, R. Xu, and B. Yan, "Integrated dipole antenna with bandwidth enhancement for terahertz waveguide-to-CPWG transition," *IEEE Antennas Wireless Propag. Lett.*, vol. 19, no. 12, pp. 2433–2436, Dec. 2020.

[9] Y. Liu *et al.*, "Millimeter-wave and terahertz waveguide-fed circularly polarized antipodal curvedly tapered slot antennas," *IEEE Trans. Antennas Propag.*, vol. 64, no. 5, pp. 1607–1614, May 2016.

[10] L. Chang, Y. Li, Z. Zhang, S. Wang, and Z. Feng, "Planar air-filled terahertz antenna array based on channelized coplanar waveguide using hierarchical silicon bulk micromachining," *IEEE Trans. Antennas Propag.*, vol. 66, no. 10, pp. 5318–5325, Oct. 2018.

[11] X.-D. Deng, Y. Li, W. Wu, and Y.-Z. Xiong, "340-GHz SIW cavity-backed magnetic rectangular slot loop antennas and arrays in silicon technology," *IEEE Trans. Antennas Propag.*, vol. 63, no. 12, pp. 5272–5279, Dec. 2015.

[12] L.-M. Si, Y. Liu, H.-D. Lu, H.-J. Sun, X. Lv, and W. Zhu, "Experimental realization of high transmittance THz 90°-bend waveguide using EMXT structure," *IEEE Photon. Technol. Lett.*, vol. 25, no. 5, pp. 519–522, Mar. 2013.

[13] Y. Liu, L.-M. Si, S.-H. Zhu, and H. Xin, "Experimental realisation of integrated THz electromagnetic crystals (EMXT) H-plane horn antenna," *Electron. Lett.*, vol. 47, no. 2, pp. 80–82, 2011.

[14] W. Withayachumnankul, R. Yamada, C. Fumeaux, M. Fujita, and T. Nagatsuma, "All-dielectric integration of dielectric resonator antenna and photonic crystal waveguide," *Opt. Exp.*, vol. 25, no. 13, pp. 14 706–14 714, 2017.

[15] W. Withayachumnankul, R. Yamada, M. Fujita, and T. Nagatsuma, "All-dielectric rod antenna array for terahertz communications," *APL Photon.*, vol. 3, no. 5, 2018, Art. no. 051707.

[16] D. Headland, W. Withayachumnankul, R. Yamada, M. Fujita, and T. Nagatsuma, "Terahertz multi-beam antenna using photonic crystal waveguide and Luneburg lens," *APL Photon.*, vol. 3, no. 12, 2018, Art. no. 126105.

[17] W. Gao, X. Yu, M. Fujita, T. Nagatsuma, C. Fumeaux, and W. Withayachumnankul, "Effective-medium-cladded dielectric waveguides for terahertz waves," *Opt. Exp.*, vol. 27, no. 26, pp. 38 721–38 734, 2019.

[18] W. Gao *et al.*, "Characteristics of effective-medium-clad dielectric waveguides," *IEEE Trans. THz Sci. Technol.*, vol. 11, no. 1, pp. 28–41, Jan. 2021.

[19] H.-T. Zhu, Q. Xue, J.-N. Hui, and S. W. Pang, "A 750-1000 GHz H-plane dielectric horn based on silicon technology," *IEEE Trans. Antennas Propag.*, vol. 64, no. 12, pp. 5074–5083, Dec. 2016.

[20] A. V. Subashiev and S. Luryi, "Modal control in semiconductor optical waveguides with uniaxially patterned layers," *J. Lightw. Technol.*, vol. 24, no. 3, pp. 1513–1522, Mar. 2006.

[21] J. Dai, J. Zhang, W. Zhang, and D. Grischkowsky, "Terahertz time-domain spectroscopy characterization of the far-infrared absorption and index of refraction of high-resistivity, float-zone silicon," *J. Opt. Soc. Amer. B*, vol. 21, no. 7, pp. 1379–1386, 2004.

[22] A. R. Mallahzadeh and S. Esfandiarpour, "Wideband H-plane horn antenna based on ridge substrate integrated waveguide (RSIW)," *IEEE Antennas Wireless Propag. Lett.*, vol. 11, pp. 85–88, 2012.